npj | climate and atmospheric science

www.nature.com/npjclimatsci

ARTICLE OPEN

Check for updates

Main drivers of Indian Ocean Dipole asymmetry revealed by a simple IOD model

Soon-Il An[1,2,3]✉, Hyo-Jin Park[2], Soong-Ki Kim[2], Wenju Cai[4], Agus Santoso[5], Daehyun Kim[6] and Jong-Seong Kug[3,7]

Indian Ocean Dipole phenomenon (IOD) refers to a dominant zonal contrast pattern of sea surface temperature anomaly (SSTA) over tropical Indian Ocean (TIO) on interannual time scales. Its positive phase, characterized by anomalously warm western TIO and anomalously cold southeastern TIO, is usually stronger than its negative phase, namely a positively skewed IOD. Here, we investigate causes for the IOD asymmetry using a prototype IOD model, of which physical processes include both linear and nonlinear feedback processes, El Nino's asymmetric impact, and a state-dependent noise. Parameters for the model were empirically obtained using various reanalysis SST data sets. The results reveal that the leading cause of IOD asymmetry without accounting seasonality is a local nonlinear process, and secondly the state-dependent noise, the direct effect by the positively skewed ENSO and its nonlinear teleconnection; the latter two have almost equal contribution. However, the contributions by each process are season dependent. For boreal summer, both local nonlinear feedback process and the state-dependent noise are major drivers of IOD asymmetry with negligible contribution from ENSO. The ENSO impacts become important in boreal fall, along with the other two processes.

npj Climate and Atmospheric Science (2023)6:93 ; https://doi.org/10.1038/s41612-023-00422-2

INTRODUCTION

The Indian Ocean Dipole/Zonal mode (IOD/IOZM) is a dominant interannual phenomenon in the tropical Indian Ocean (TIO)[1–4]. The IOD is characterized by a dipole pattern of SST anomalies between the southeastern tropical TIO and the western tropical TIO (Fig. 1)[5], and drives a pronounced climate impact on East Africa, western Indonesia, Australia, India, and many other regions[6–12]. The IOD is developed by either internal air-sea interaction or external forcing such as El Niño–Southern Oscillation (ENSO). Its evolution follows a seasonal march, namely, starting during boreal summer, reaching a peak during fall, and decaying rapidly during winter[1,4]. It has been known that not only ENSO triggers an IOD, but also an IOD influences the development and decay of ENSO[13–18].

The IOD grows through the internal feedback processes, external drivers, and stochastic forcing such as weather noise[5,19], where internal feedback processes include the wind-thermocline-SST (WTS) feedback[1,20], the wind-evaporation-SST (WES) feedback[21], and cloud-radiation-SST feedback[22,23], and the external drivers include ENSO[4,23,24], the southern annular mode[25], Indo-Pacific warm pool[3,26], and the Indonesian Throughflow[27]. These growing mechanisms do not necessarily equally exert on positive IOD and negative IOD phases. The Indian Ocean dipole mode index (DMI)[1] (Fig. 1c) is positively skewed. The DMI is defined as the difference in SST anomalies between the western TIO (50°E to 70°E and 10°S to 10°N; IODW) and the southeastern TIO (90°E to 110°E and 10°S to 0°S; IODE). While the skewness of SSTA over the southeastern TIO (IODE) is greater than that over the western TIO (IODW), it does not necessarily mean that the skewness of DMI is primarily determined by IODE. The skewness of DMI is determined by a combination of the SST variations of each pole, rather than being determined solely by the sum of their individual skewness values.

Asymmetry in IOD leads to asymmetry in the impact on precipitation[28,29] and marine ecosystems[30] through an asymmetric atmospheric response to SST anomalies. Like in ENSO asymmetry[31–35], the nonlinear dynamical heating, especially zonal and vertical nonlinear thermal advections had been proposed as a cause of asymmetry of the IOD[11,36], which amplifies the positive IOD and damps the negative IOD[37,38]. Nonlinear thermocline feedback associated with an asymmetric feedback between thermocline and SST especially over the southeastern TIO was also suggested for causing positive skewness of the DMI[39]. As a thermodynamical cause, asymmetry of SST-cloud-radiation feedback was proposed since as the SST decreases, this feedback is capped due to convective threshold[37,38,40], but other studies[41–43] argued that this feedback rather weakens the asymmetry. The SST biases in ocean assimilation data caused such opposite results[41].

In addition to internal nonlinear feedback process, the external process, especially asymmetric ENSO impact on IOD could lead the asymmetry of IOD in two ways. First, the coherence between El Niño (La Niña) and the positive (negative) IOD may contribute to the positive skewness of the IOD, because the amplitude of El Niño is significantly larger than the amplitude of La Niña[31,33,44–46]. Second, the phase-dependent teleconnection of ENSO on the IOD can also contribute to IOD asymmetry because the El Niño teleconnection on the positive IOD is greater than La Niña teleconnection on negative IOD (see Supplementary Fig. 1 and ref. [41]).

The role of state-dependent noise on asymmetry characteristics of ENSO has been proposed[47,48], although its actual contribution was argued as secondary, i.e., less than nonlinear dynamical

[1]Irreversible Climate Change Research Center, Yonsei University, Seodaemun-gu, Seoul 03722, Republic of Korea. [2]Department of Atmospheric Sciences, Yonsei University, Seodaemun-gu, Seoul 03722, Republic of Korea. [3]Division of Environmental Science and Engineering, Pohang University of Science and Technology (POSTECH), Pohang, Republic of Korea. [4]CSIRO Environment, Aspendale, VIC 3195, Australia. [5]Australian Research Council (ARC) Centre of Excellence for Climate Extremes, and Climate Change Research Centre, The University of New South Wales, Sydney, NSW 2052, Australia. [6]Department of Atmospheric Sciences, University of Washington at Seattle, Seattle, WA, USA. [7]Institute for Convergence Research and Education in Advanced Technology, Yonsei University, Seoul 03722, Republic of Korea.
✉email: sian@yonsei.ac.kr

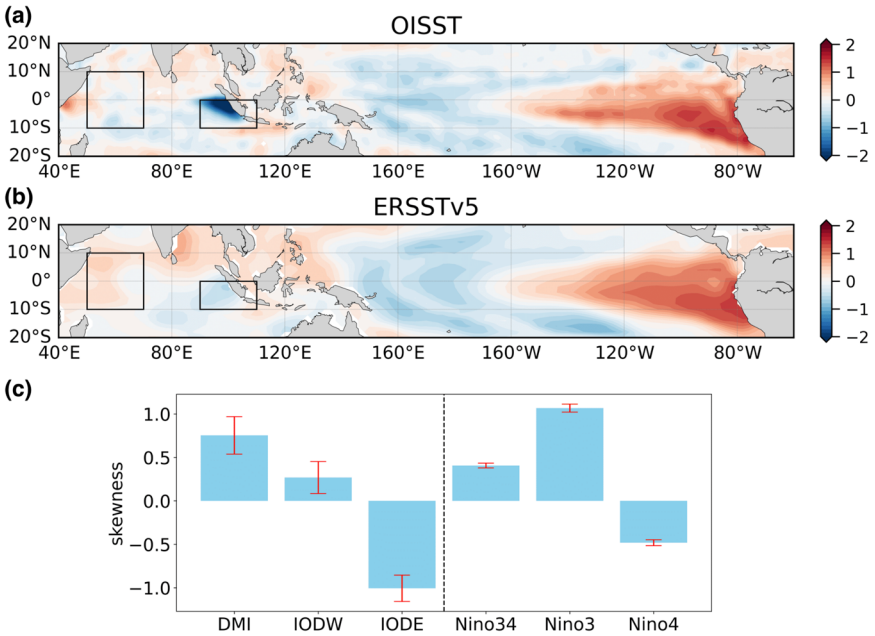

Fig. 1 Skewness of tropical Ocean SST anomalies. Skewness of SST anomalies over tropical Indian (SON season) and Pacific oceans (DJF season) obtained from **a** OISST and **b** ERSSTv5. Scale bars in Skewness are in the right side of each panel. **c** Skewness of DMI (IODW minus IODE), IODW (SSTA averaged over western box in TIO), IODE (SSTA averaged over eastern box in TIO), Nino3.4 (SSTA over 5°S-5°N, 170°W-120°W), Nino3 (SSTA over 5°S-5°N, 150°W-90°W) and Nino4 (SSTA over 5°S-5°N, 160°E-150°W) indices. **c** is obtained from multi-product ensemble of six different reanalysis data sets (ERSSTv5, HadISST, OISST, ORAS5, SODA, GODAS). Red error bar indicates the inter-product spread corresponding to one standard deviation. Units in Skewness are normalized third moment so dimensionless.

process[49]. Similarly, the dependency of atmospheric noise on the IOD was reported in that the variability from synoptic eddies to Madden-Julian Oscillation (MJO)[50] over central-eastern TIO was significantly weakened during the positive IOD phase[51,52]. The high-frequency atmospheric variability is suppressed by anomalous vertical westerly wind shear associated with positive IOD, especially during the developing phase of a positive IOD[51], while it becomes more active during the developing phase of a negative IOD; furthermore, a possibility of an upscale feedback in the IOD from high-frequency atmospheric variability to the IOD was suggested. Similarly, MJO events showed a weaker convection and less organized wind anomalies during the positive IOD because of the reduced low-level humidity and opposite case is also true during the negative IOD[52]. Atmospheric intraseasonal disturbances associated with equatorial westerly zonal winds involve a quick termination of an IOD by generating anomalous downwelling Kelvin waves[53]. Therefore, such multiplicative noise forcing is supposed to play some role in modifying an IOD.

As mentioned above, many studies proposed mechanisms on asymmetry of the IOD, but their relative and collective roles have not been quantified so far. In this study, we developed a nonlinear version of the simple IOD model to explore the origin of asymmetry of the IOD, of which a linear version has been used for the study of origin of the IOD growth mechanism[5]. Nonlinear process is necessary to understand asymmetry of the IOD as mentioned above. Therefore, the linear IOD model needs to be expanded as a nonlinear model, in which both deterministic and stochastic nonlinearities are incorporated, and the nonlinear model is used for analyzing the role of various processes in the asymmetry of the IOD quantitatively.

RESULTS

IOD asymmetry in various ocean reanalysis data sets

In this study, we utilize six ocean analysis data sets, which span from 1982 to 2015 (Methods). Asymmetry of the IOD was measured by skewness of SST anomalies[31]. The spatial skewness pattern of SST anomalies over the TIO obtained from OISST shows a moderate positive skewness over the western TIO and a strong negative skewness over the southeastern TIO (Fig. 1a). A similar pattern but with smaller amplitude is also observed from ERSSTv5 (Fig. 1b). Other data sets also show a broadly similar pattern (not shown). Skewness of area-averaged SST anomalies over the TIO obtained from various ocean reanalysis data sets show a somewhat wide inter-data spread (Fig. 1c and Supplementary Fig. 2). Maximum skewness of the DMI for the boreal fall season (September – November; SON) among six data sets was 1.06 (OISST) and the minimum was 0.36 (ERSSTv5). On the other hand, the inter-data spread in skewness of ENSO indices is small (Fig. 1c and Supplementary Fig. 2). Such discrepancy between the Indian Ocean and the Pacific may be related to the much longer moored buoy observation data in tropical Pacific through Tropical Pacific Observing System (TPOS) since 1985[54,55] compared to the Indian Ocean. In the Indian Ocean, a basin-scale moored buoy array program called RAMA, which refers to Research Moored Array for African-Asian-Australian Monsoon Analysis and Prediction, was initiated in 2000[56]. Understanding the reasons for discrepancy in inter-product spread between the Pacific and Indian Ocean is beyond the scope of this study. Here we used all six data sets with an equal weighting (Methods). We highlight that the skewness of the DMI is dominated by the southeastern TIO SST anomalies (Fig. 1c).

IOD asymmetry reproduced by using a nonlinear IOD model

To investigate the cause of the IOD asymmetry, we updated the linear IOD model[5] to the nonlinear version as follows;

$$\frac{\partial T}{\partial t} = \lambda_m T + \beta_{1,m} E(t) + \beta_{2,m} E(t)^2 + \gamma_m T^2 + \sigma_m (1 + B_m T)\xi_t \quad (1)$$

Where T is DMI (°C); $E(t)$ is ENSO forcing (i.e., Nino3.4 index); and ξ_t is a Gaussian white noise with a zero mean and unitary standard deviation. Physically, λ_m, $\beta_{1,m}$, $\beta_{2,m}$, γ_m, σ_m and B_m respectively

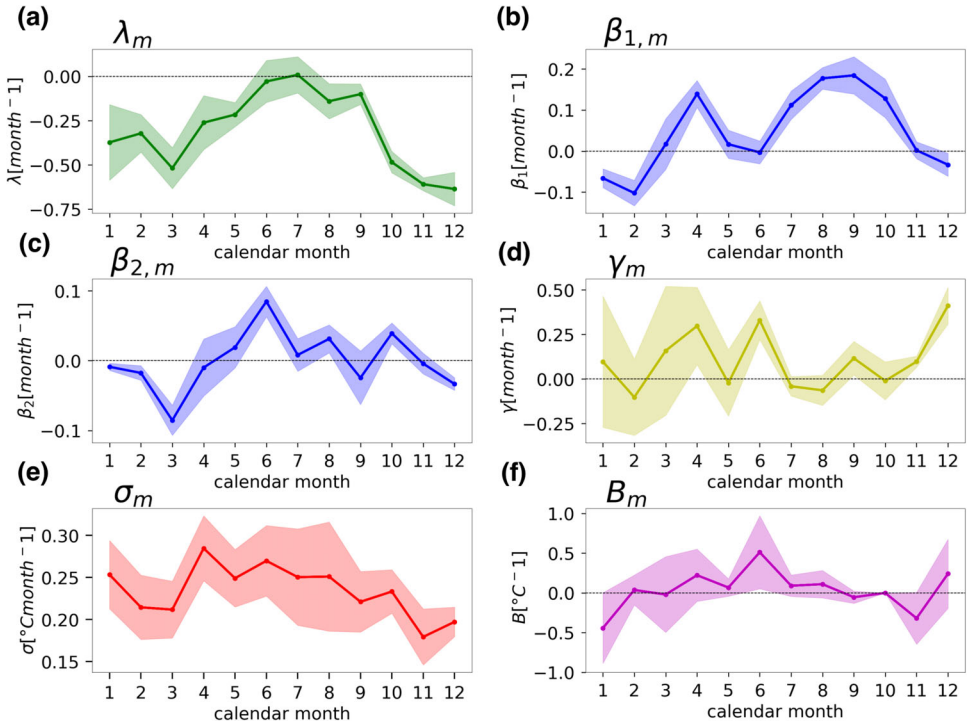

Fig. 2 Parameters of IOD model. Annual changes in parameters of the nonlinear IOD model. **a** $\boldsymbol{\lambda_m}$, (**b**) $\boldsymbol{\beta_{1,m}}$, (**c**) $\boldsymbol{\beta_{2,m}}$, (**d**) $\boldsymbol{\gamma_m}$, (**e**) $\boldsymbol{\sigma_m}$, and (**f**) $\boldsymbol{B_m}$. Solid lines are ensemble-mean of each parameter obtained from six reanalysis data and the shading represents one-standard ensemble spread of inter-data. Units are indicated in the left of each panel.

represent parameters for a comprehensive local linear feedback, ENSO-driven linear impact on the IOD, ENSO-driven nonlinear impact on the IOD, comprehensive local nonlinear feedback, amplitude of stochastic forcing, and the IOD state-dependent noise (see Introduction and ref. [5]). Each parameter was computed on each calendar month, indicated by the subscript m, for each dataset. The temporal correlation between the actual DMI and the reproduced DMI only by the deterministic components (i.e., without stochastic forcing) where the initial condition of this simulation was arbitrary chosen and ENSO forcing was prescribed at each time step, was 0.48 ± 0.027 (mean of six datasets $\pm$ one standard deviation), which is mainly attributed to a close relationship between IOD and ENSO. Nevertheless, this correlation is higher than that between actual DMI and Nino-3.4 index, that is 0.35 ± 0.019.

The parameter λ_m shows a strong annual cycle with a predominantly negative value for the whole year except for July (Fig. 2a), indicating a linear damping (or linear stability), which is weakest in June to September, the typical growth phase of the IOD. This annual evolution of linear damping would maximize the IOD around October, because a crossing from above mean of λ_m to below mean occurs between September and October. $\beta_{1,m}$ is mostly positive except for boreal winter, and it shows a kind of semi-annual cycle with April and September peaks (Fig. 2b). These two peaks indicate that the ENSO may have both triggering (April) and amplifying (September) effects on the IOD. $\beta_{2,m}$ shows overall the positive values from May to November with the maximum in June (Fig. 2c), and thus asymmetry in ENSO-teleconnection on the IOD is the most dominant during June. γ_m does not exhibit apparent annual and semi-annual features (Fig. 2d) with peaks in April, June, September and December, and the inter-data spread is quite large, especially from January to May. σ_m is positive for throughout the year (Fig. 2e), thus consistently contributing to the enhancement of the IOD variability. Especially high σ_m during the boreal spring to summer may be associated with initiation of the IOD by a stochastic forcing. B_m shows a positive peak in June (Fig. 2f), which can increase skewness of a system[57]. However, the positive B_m appears to contradict the previously suggested tendency of weak and strong high-frequency atmospheric variability (synoptic to intraseasonal timescale) during the positive and negative IOD events, respectively[51]. This is because the stochastic forcing in this study is not explicitly diagnosed as the actual high-frequency atmospheric variability, but as a residual. This point is discussed in the last section.

To understand the reason for each parameter's annual features, a mixed layer heat budget analysis would be required. However, that is not the main purpose of our study, which shall be left for others or a future study. Instead, our present focus is to examine whether our statistical IOD model works well to capture the observed IOD's statistical properties.

As shown in Fig. 3, variance and skewness* of the DMI at each calendar month obtained from the IOD model closely resemble those from the six reanalysis data sets. Here, we use the non-normalized third moment (denoted skewness*) instead of skewness (i.e., normalized third moment), because of strongly exaggerated skewness by too small variance during the winter season. Note that the ensemble-mean maximum skewness* occurs in November in the reanalysis data but in October in the model, and the overall skewness* is slightly underestimated by the model. Nonetheless, the results verifies that this simple IOD model is capable to reproduce the reanalysis IOD properties with a good degree of fidelity.

Main driver of IOD asymmetry

To find the main drivers of the IOD asymmetry, we conducted sensitivity experiment using the nonlinear IOD model, in which we turn off one process at a time while all others are left on. By doing so, we could quantify each process's contribution to variance and skewness. Variance and skewness of DMI for all seasons obtained from six reanalysis data are 0.211 and 0.688, respectively; and the reproduced variance and skewness of the DMI by the simple IOD

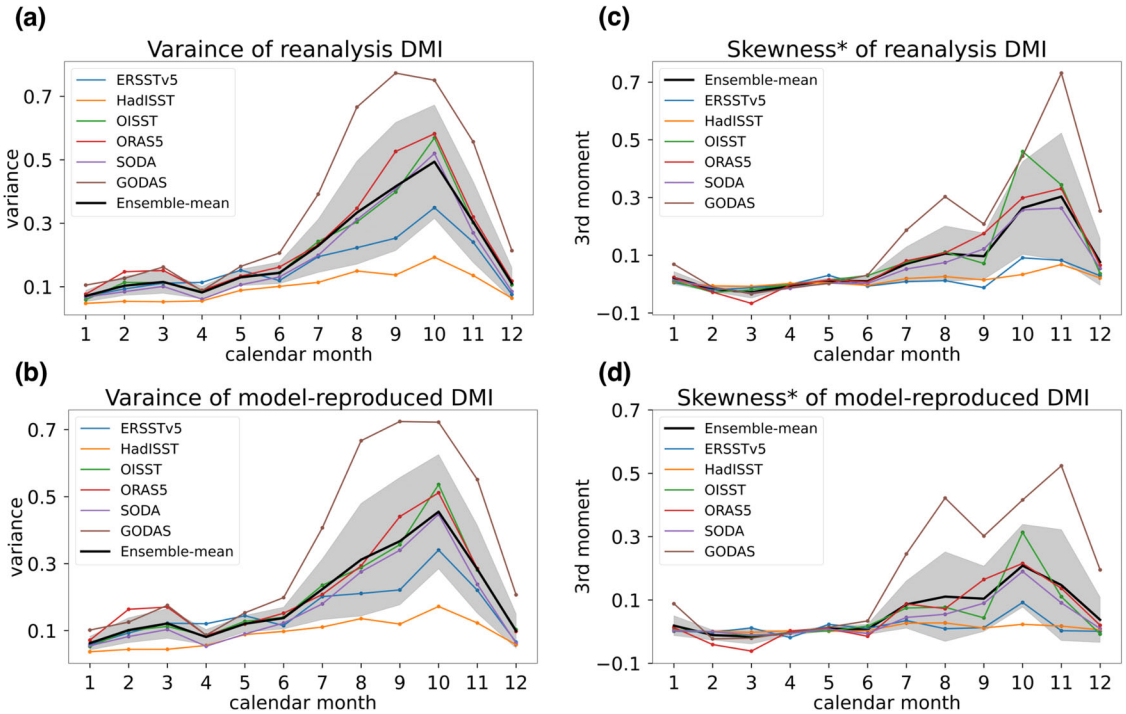

Fig. 3 Variance and Skewness of observed and model-reproduced DMI. Ensemble-mean (black curve) and ensembles of (**a**, **b**) variance (second moment) and (**c**, **d**) skewness* (third moment) of DMI for each calendar month. **a**, **c** From reanalysis data and **b**, **d** from the IOD model. The shading represents one-standard ensemble spread of the six-reanalysis data (**a**, **c**) and the model-reproduced quantities (**b**, **d**). In (**b**, **d**), 'ERSSTv5' indicates the model-reproduced output using parameters obtained from ERSSTv5; and likewise other data sets. Skewness* indicates the third moment without normalization.

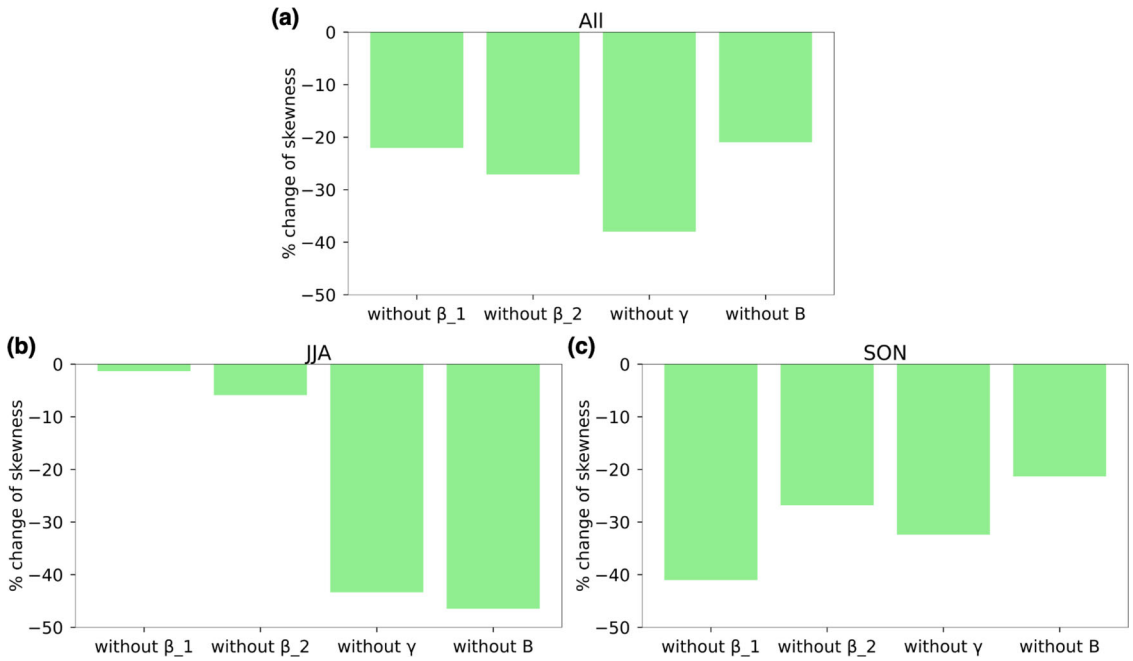

Fig. 4 Model sensitivity in DMI skewness to each parameter. Changing rate (%) in skewness by removing one of processes in the nonlinear IOD model against that with whole processes. Averages for **a** all months, **b** June-August and **c** September-November. Omitted parameters are indicated in *x*-axis. Larger the negative values indicate stronger its effect in inducing IOD asymmetry.

model are 0.204 and 0.596, respectively. That is, 97% of the actual variance and 87% of the actual skewness are reproduced, indicating the nonlinear IOD model works very well.

Here, we focus on sensitivity experiment for four parameters ($\beta_{1,m}$, $\beta_{2,m}$, γ_m, B_m) which influences the IOD asymmetry. Without $\beta_{1,m}$, which measures a direct impact of ENSO, variance of the DMI was reduced by 21.4% (Supplementary Fig. S3), and skewness of the DMI was also reduced by 22.04% of their corresponding reproduced values (Fig. 4a). This suggests that ENSO directly and notably contributes to both DMI variance and skewness. Without $\beta_{2,m}$, on the other hand, the DMI variance was not changed much (4.6% reduction), but the DMI skewness was reduced by 27.07%,

suggesting that ENSO-induced asymmetric teleconnection effect does not significantly influence IOD amplitude but induces positively skewed IOD. Similarly, without γ_m (nonlinear local feedback) and B_m (state-dependent noise), there was little change in DMI variance (3.6% and 1.6% reduction, respectively), but large reduction in the DMI skewness of 38.0% and 21.0%, respectively. In summary, all four process terms play a role in driving the skewness of DMI. Specifically, the nonlinear local feedback (γ_m) is the primary driver, and ENSO-induced asymmetric teleconnection ($\beta_{2,m}$) is secondary along with the state-dependent noise (B_m) and ENSO's direct impact due to positively skewed properties of ENSO. The three nonlinear processes ($\beta_{2,m}$, γ_m, B_m) do not play appreciable role in modifying DMI variance (Supplementary Fig. S3).

The relative contribution to IOD asymmetry by each process varies with season (Fig. 4b, c). For JJA (June to August), skewness of the DMI without each of the four parameters ($\beta_{1,m}$, $\beta_{2,m}$, γ_m, B_m) was reduced by 1.4, 5.9, 43.3 and 46.5% of the reproduced skewness, respectively. While for SON (September to November), skewness of DMI without four parameters ($\beta_{1,m}$, $\beta_{2,m}$, γ_m, B_m) was reduced by 41.0, 26.8, 32.4 and 21.4% of the reproduced skewness, respectively. Here, we do not discuss boreal winter and spring cases because of the small skewness* of the DMI in these seasons (Fig. 3). As we expect, for the boreal summer, because of relatively stronger local air-sea coupling, the roles of γ_m and B_m are dominant; and for the boreal fall, as ENSO continues to grow, the role of the ENSO on DMI skewness through parameters, $\beta_{1,m}$ and $\beta_{2,m}$, becomes larger than in summer.

DISCUSSION

In this study, a prototype nonlinear IOD model was developed, which reveals the origin of IOD's amplitude asymmetry quantitatively. This model incorporates both linear processes as documented in the previous studies[5,19] and nonlinear processes which include a comprehensive local nonlinear feedback, ENSO-driven nonlinear teleconnection effect on IOD, and state-dependent noise forcing. The IOD model well reproduced the observed IOD variance and skewness, as well as their seasonality. Therefore, to quantitatively evaluate the contribution of each process to IOD asymmetry, we use the nonlinear IOD model that is difficult to diagnose directly from observations. By performing sensitivity experiments in which one of these processes is switched off, we found that the local nonlinear feedback is the primary factor for the IOD asymmetry. However, the dependency of the IOD asymmetry on each nonlinear process displays seasonal variation such that for the boreal summer, local nonlinear feedback and state-dependent noise have the largest impact with almost equal contribution, and the impact of ENSO is negligible; for the boreal fall, the direct effect of ENSO teleconnection (i.e., El Niño-La Niña asymmetry) plays the most important role, yet the impact of the local nonlinear feedback is still comparably important. In this study, we could not specify which local feedback process is the most responsible for growth and asymmetry of IOD because the comprehensive local linear and nonlinear feedbacks were estimated empirically. To explore this, a detailed heat budget analysis is required.

There are a couple of caveats. First and foremost, the orthogonality between two different terms was not strictly held. Physically this is not a problem because the processes are linked to each other, and the intrinsic nonlinearity can lead to interaction between two different processes. However, in terms of quantifying each process in driving IOD skewness based on the sensitivity experiments, it would be cleaner if each process were to be independent. For reliability test, we performed the same experiment as in Fig. 4 except that we retained a half of one of parameters at a time. The % change in skewness of DMI shows a reduction in a somewhat linear fashion compared to the original sensitivity experiment (Supplementary Fig. S4). Additional experiments, in which values of two parameters are reduced to be half at the same time, also produced quite similar % change in both variance and skewness of DMI compared to a simple sum of each corresponding parameter's effect (Supplementary Fig. S5). Therefore, these results support that our approach to quantify individual effect of each process is quite reasonable. Second, the physical mechanism on the state-dependent process has not been fully unveiled so far. Detailed heat budget analysis may give us some clues on how state-dependent process works. Furthermore, the noise forcing term was computed not directly from the weather noise data (i.e., short-interval data) but from the residual after fitting the monthly-mean data, and thus the noise forcing in this study includes all other processes resolved in monthly timescale, which are not explicitly formulated as deterministic processes in Eq. (1). Atlantic ocean's impact on IOD may be one of these factors[58–60]. Nevertheless, the current IOD model explains 97% of the actual variance and 87% of the actual skewness, and thus our results are quite reliable.

Notwithstanding this nonlinear IOD model is applicable in many aspects. First, it can be used for IOD prediction. In this case, the initial conditions and ENSO index should be carefully considered. Second, it can also be utilized for understanding IOD amplitude and asymmetry in climate models. By computing parameters in this IOD model using the climate model outputs, we could get clues on how IOD amplitude and asymmetry vary, and which physical processes are dominant in driving them across models; and how the IOD is related to ENSO in the climate models. For example, IOD skewness (and ENSO asymmetry) tends to be underestimated in most climate models[61,62], then using this IOD model we can understand to what extent this underestimation is due to local processes vs ENSO teleconnection. The results imply that reducing IOD skewness bias would require reducing ENSO asymmetry bias, not just biases within the Indian Ocean. Third, this model can be used for understanding decadal variation of the IOD and its linkage to ENSO[63,64]. From this application, we could answer as to whether the decadal modulations of IOD characteristics are due to the background condition change in tropical Indian Ocean or change in ENSO itself.

METHODS

Ocean reanalysis data

In this study, six different ocean temperature products with monthly resolution were utilized.

1. ERSST (Extended Reconstructed Sea Surface Temperature Version 5)[65] is a global monthly SST reconstruction based on ICOADS SST anomalies with $2° \times 2°$ horizontal resolution starting from 1854. The newest version of ERSST version 5, uses new datasets from ICOADS Release 3.0 (SST), coming from Argo floats above 5 meters, Hadley Centre Ice-SST version 2 (HadISST2) ice concentration.
2. HadISST (Hadley Center Global Sea Ice and Sea Surface Temperature Version 1.1)[66] is an SST analysis with a horizontal resolution of $1° \times 1°$ starting from 1870. It was built on an EOF-based Reduced Space Optimal Interpolation (RSOI) technique, using SST observations from ICOADS, the Met Office Marine Data Bank (MDB), and satellite products (1982 onward). Noninterpolated observed SST anomalies were then superimposed onto the reconstructed SST to improve the localized variability.
3. OISST (NOAA Optimum Interpolation SST version 2)[67] based on satellite products and in situ data from ships and buoys is constructed using Optimum Interpolation technique with a horizontal resolution of $1° \times 1°$ grids starting from 1982. This product is regarded as most accurate and reliable to the observations.

4. ORA-S5 (European Center for Medium-Range Weather Forecasts Ocean Reanalysis System 5)[68] is a historical reconstruction of the ocean and sea-ice state built on the ECMWF OCEAN5 system, new global eddy-permitting ocean-sea ice ensemble reanalysis system. This product includes 5 ensemble members (the member used in this study is named "opa0" with a resolution of $1° \times 1°$) and starting from 1979. ORA-S5 also assimilates an in-situ temperature and salinity data set named EN4, which includes all conventional oceanic observations like Argo, moored buoys, and ship measurements, except using an ocean model with a horizontal resolution approximately 25 km in the tropics and 75 vertical levels.
5. SODA (Simple Ocean Data Assimilation version version 3.3.1)[69] based on the Modular Ocean Model (MOM) version 5 with finer a horizontal resolution of $0.5° \times 0.5°$ and a vertical resolution of 50- levels was also used. SODA 3.3.1 is forced by MERRA2 and spanning the 36-year period 1980–2015. The observations used in SODA include the World Ocean Database of historical hydrographic profiles, in-situ SST from the International Comprehensive Ocean-Atmosphere Data Set (ICOADS), and satellite data. The potential temperature at 5 m is used to represent the SST.
6. GODAS (National Centers for Environmental Prediction Global Ocean Data Assimilation System)[70] is a reanalysis based on a quasi-global configuration of MOM Version 3 (MOM3) with a horizontal resolution of $1° \times 1°$, enhanced to 1/3° in latitude within 10° of the equator, and 40 vertical levels, and it started from 1980. GODAS has assimilated observations from the Tropical Atmosphere Ocean (TAO) TRITON and PIRATA mooring and Argo profiling floats etc. The potential temperature at 5 m is used to represent the SST.

This study focuses on the time period of 1982–2015, during which all products are available.

Parameter computations

In Eq. (1), parameters λ_m, $\beta_{1,m}$, $\beta_{2,m}$ and γ_m are calculated using the DMI and Nino3.4 indices obtained from 6 ocean reanalysis datasets by applying a least-square method at each calendar month. σ_m is calculated as a standard deviation of the residual. B_m is calculated by using optimization method so that residual/$\sigma_m(1 + B_m T)$ follows a gaussian distribution. The subscript 'm' indicates the calendar month ($m = 1,\ldots,12$), and the parameters are calculated separately for each calendar month. After that, using the fitted parameters, the DMI was reproduced by integrating the model (1).

Model experiments

DMI was reproduced by solving the stochastic differential equation. Gaussian random number ($\xi_t \sim N(0,1)$) was inputted as stochastic forcing term. Euler-Maruyama scheme, the simplest and most common scheme, was used. The simple model was integrated with the same length as actual DMI and 10,000 DMI timeseries (10,000 noise ensemble) were reproduced by inputting another gaussian noise. The initial values were set to them of the actual DMI. Finally, the statistics (variance and skewness) simulated by the conceptual model were obtained as the mean of them calculated for each noise ensembles.

DATA AVAILABILITY

ERSSTv5 is available from https://psl.noaa.gov/data/gridded/data.noaa.ersst.v5.html; the HadISST from https://www.metoffice.gov.uk/hadobs/hadisst/; the OISST https://psl.noaa.gov/data/gridded/data.noaa.oisst.v2.highres.html; the ORAS5 https://cds.climate.copernicus.eu/cdsapp#!/dataset/reanalysis-oras5?tab=form; the SODA https://www2.atmos.umd.edu/~ocean/index_files/soda3.3.1_mn_download.htm; the GODAS https://psl.noaa.gov/data/gridded/data.godas.html.

CODE AVAILABILITY

Any codes used in the manuscript are available upon request from H Park, hjpark1021@yonsei.ac.kr.

Received: 22 December 2022; Accepted: 5 July 2023;
Published online: 15 July 2023

REFERENCES

1. Saji, N., Goswami, B., Vinayachandran, P. & Yamagata, T. A dipole mode in the Tropical Ocean. *Nature* **401**, 360–363 (1999).
2. Webster, P. J., Moore, A. M., Loschnigg, J. P. & Leben, R. R. Coupled ocean-atmosphere dynamics in the Indian Ocean during 1997–98. *Nature* **401**, 356–360 (1999).
3. Annamalai, H. et al. Coupled dynamics over the Indian Ocean: Spring initiation of the Zonal Mode. *Deep Sea Res. 2 Top. Stud. Oceanogr.* **50**, 2305–2330 (2003).
4. An, S. A dynamic link between the basin-scale and zonal modes in the Tropical Indian Ocean. *Theor. Appl. Climatol.* **78**, 203–215 (2004).
5. An, S.-I. et al. Intensity changes of Indian Ocean dipole mode in a carbon dioxide removal scenario. *NPJ Clim. Atmos. Sci.* **5**, 20 (2022).
6. Ashok, K., Guan, Z. & Yamagata, T. Impact of the Indian Ocean dipole on the relationship between the Indian monsoon rainfall and ENSO. *Geophys. Res. Lett.* **28**, 4499–4502 (2001).
7. Black, E., Slingo, J. & Sperber, K. R. An observational study of the relationship between excessively strong short rains in coastal East Africa and Indian ocean SST. *Mon. Weather Rev.* **131**, 74–94 (2003).
8. Clark, C. O., Webster, P. J. & Cole, J. E. Interdecadal variability of the relationship between the Indian Ocean zonal mode and East African coastal rainfall anomalies. *J. Clim.* **16**, 548–554 (2003).
9. Zubair, L., Rao, S. A. & Yamagata, T. Modulation of Sri Lankan Maha rainfall by the Indian Ocean Dipole. *Geophys. Res. Lett.* **30**, 1063 (2003).
10. Saji, N. H. & Yamagata, T. Possible impacts of Indian Ocean Dipole mode events on global climate. *Clim. Res.* **25**, 151–169 (2003).
11. Cai, W. et al. Increased frequency of extreme Indian ocean dipole events due to greenhouse warming. *Nature* **510**, 254–258 (2014).
12. Luo, J.-J. et al. Current status of intraseasonal–seasonal-to-interannual prediction of the indo-pacific climate. World Scientific, Singapore, 63–107 (2016).
13. Kug, J. S., Kirtman, B. P. & Kang, I. S. Interactive feedback between ENSO and the Indian Ocean in an interactive ensemble coupled model. *J. Clim.* **19**, 6371–6381 (2006).
14. Kug, J. S. et al. Role of the ENSO-Indian Ocean coupling on ENSO variability in a coupled GCM. *Geophys. Res. Lett.* **33**, 2–5 (2006).
15. Izumo, T. et al. Influence of the state of the Indian Ocean Dipole on the following years El Nĩno. *Nat. Geosci.* **3**, 168–172 (2010).
16. Luo, J. J. et al. Interaction between El Niño and extreme Indian Ocean dipole. *J. Clim.* **23**, 726–742 (2010).
17. Kim, J. W. & An, S. Western North Pacific anticyclone change associated with the El Niño–Indian Ocean Dipole coupling. *Int. J. Climatol.* **39**, 2505–2521 (2019).
18. Le, T., Ha, K. J., Bae, D. H. & Kim, S. H. Causal effects of Indian Ocean Dipole on El Niño-Southern Oscillation during 1950–2014 based on high-resolution models and reanalysis data. *Environ. Res. Lett.* **15**, 1040b6 (2020).
19. Stuecker, M. F. et al. Revisiting ENSO/Indian Ocean Dipole phase relationships. *Geophys. Res. Lett.* **44**, 2481–2492 (2017).
20. Bjerknes, J. Monthly weather reyiew atmospheric teleconnections from the equatorial pacific. *Mon. Weather Rev.* **97**, 163–172 (1969).
21. Xie, S.-P. & Philander, S. G. H. A coupled ocean-atmosphere model of relevance to the ITCZ in the eastern Pacific. *Tellus, Ser. A* **46 A**, 340–350 (1994).
22. Li, T., Wang, B., Chang, C. P. & Zhang, Y. A theory for the Indian Ocean dipole-zonal mode. *J. Atmos. Sci.* **60**, 2119–2135 (2003).
23. Fischer, A. S., Terray, P., Guilyardi, E., Gualdi, S. & Delecluse, P. Two independent triggers for the Indian Ocean dipole/zonal mode in a coupled GCM. *J. Clim.* **18**, 3428–3449 (2005).
24. Yang, Y. et al. Seasonality and predictability of the Indian Ocean dipole mode: ENSO forcing and internal variability. *J. Clim.* **28**, 8021–8036 (2015).
25. Lau, N. C. & Nath, M. J. Coupled GCM simulation of atmosphere-ocean variability associated with zonally asymmetric SST changes in the tropical Indian Ocean. *J. Clim.* **17**, 245–265 (2004).
26. Song, Q., Vecchi, G. A. & Rosati, A. J. Indian Ocean variability in the GFDL coupled climate model. *J. Clim.* **20**, 2895–2916 (2007).
27. Tozuka, T., Luo, J. J., Masson, S. & Yamagata, T. Decadal modulations of the Indian Ocean dipole in the SINTEX-F1 coupled GCM. *J. Clim.* **20**, 2881–2894 (2007).
28. Qiu, Y., Cai, W., Guo, X. & Ng, B. The asymmetric influence of the positive and negative IOD events on China's rainfall. *Sci. Rep.* **4**, 4943 (2014).

29. Behera, S. K. & Ratnam, J. V. Quasi-asymmetric response of the Indian summer monsoon rainfall to opposite phases of the IOD. *Sci. Rep.* **8**, 123 (2018).
30. Vallivattathillam, P. et al. Positive Indian Ocean Dipole events prevent anoxia off \hack{\break} the west coast of India. *Biogeosciences* **14**, 1541–1559 (2017).
31. An, S.-I. & Jin, F.-F. Nonlinearity and asymmetry of ENSO. *J. Clim.* **17**, 2399–2412 (2004).
32. An, S.-I., Ham, Y.-G., Kug, J.-S., Jin, F.-F. & Kang, I.-S. El Niño–La Niña asymmetry in the coupled model intercomparison project simulations. *J. Clim.* **18**, 2617–2627 (2005).
33. An, S.-I. A review of interdecadal changes in the nonlinearity of the El Niño-Southern Oscillation. *Theor. Appl. Climatol.* **97**, 29–40 (2009).
34. Kim, S.-K. & An, S.-I. Untangling El Niño-La Niña asymmetries using a nonlinear coupled dynamic index. *Geophys. Res. Lett.* **47**, e2019GL085881 (2020).
35. An, S.-I., Tziperman, E., Okumura, Y. M. & Li, T. ENSO Irregularity and Asymmetry. in *El Niño Southern Oscillation in a Changing Climate,* Vol. 253, 153–172 (John Wiley & Sons, Inc., 2020).
36. Cai, W. et al. Opposite response of strong and moderate positive Indian Ocean Dipole to global warming. *Nat. Clim. Change* **11**, 27–32 (2021).
37. Hong, C. C., Li, T., Ho, L. & Kug, J. S. Asymmetry of the Indian Ocean dipole. Part I: observational analysis. *J. Clim.* **21**, 4834–4848 (2008).
38. Hong, C. C., Li, T. & Luo, J. J. Asymmetry of the Indian Ocean dipole. Part II: model diagnosis. *J. Clim.* **21**, 4849–4858 (2008).
39. Zheng, X. T., Xie, S. P., Vecchi, G. A., Liu, Q. & Hafner, J. Indian ocean dipole response to global warming: analysis of ocean-atmospheric feedbacks in a coupled model. *J. Clim.* **23**, 1240–1253 (2010).
40. Hong, C. C., Li, T., LinHo & Chen, Y. C. Asymmetry of the Indian Ocean basinwide SST anomalies: roles of ENSO and IOD. *J. Clim.* **23**, 3563–3576 (2010).
41. Cai, W., van Rensch, P., Cowan, T. & Hendon, H. H. An asymmetry in the IOD and ENSO teleconnection pathway and its impact on australian climate. *J. Clim.* **25**, 6318–6329 (2012).
42. Cai, W. & Qiu, Y. An observation-based assessment of nonlinear feedback processes associated with the indian ocean dipole. *J. Clim.* **26**, 2880–2890 (2013).
43. Ogata, T., Xie, S. P., Lan, J. & Zheng, X. Importance of ocean dynamics for the skewness of the Indian Ocean dipole mode. *J. Clim.* **26**, 2145–2159 (2013).
44. Hoerling, M. P., Kumar, A. & Zhong, M. El Niño, La Niña, and the nonlinearity of their teleconnections. *J. Clim.* **10**, 1769–1786 (1997).
45. Burgers, G. & Stephenson, D. B. The "normality" of El Niño. *Geophys. Res. Lett.* **26**, 1027–1030 (1999).
46. Jin, F.-F., An, S.-I., Timmermann, A. & Zhao, J. Strong El Niño events and nonlinear dynamical heating. *Geophys. Res. Lett.* **30**, 20–21 (2003).
47. Levine, A. F. Z. & Jin, F.-F. Noise-induced instability in the ENSO recharge oscillator. *J. Atmos. Sci.* **67**, 529–542 (2010).
48. Levine, A., Jin, F. F. & McPhaden, M. J. Extreme noise–extreme El Niño: how state-dependent noise forcing creates El Niño–La Niña asymmetry. *J. Clim.* **29**, 5483–5499 (2016).
49. An, S.-I., Kim, S.-K. & Timmermann, A. Fokker–Planck dynamics of the El Niño-Southern Oscillation. *Sci. Rep.* **10**, 16282 (2020).
50. Madden, R. A. & Julian, P. R. Detection of a 40–50 Day Oscillation in the Zonal Wind in the Tropical Pacific. *J. Atmos. Sci.* **28**, 702–708 (1971).
51. Kug, J. S., Sooraj, K. P., Jin, F. F., Luo, J. J. & Kwon, M. Impact of Indian Ocean Dipole on high-frequency atmospheric variability over the Indian Ocean. *Atmos. Res.* **94**, 134–139 (2009).
52. Wilson, E. A., Gordon, A. L. & Kim, D. Observations of the madden julian oscillation during Indian ocean dipole events. *J. Geophys. Res. Atmospheres* **118**, 2588–2599 (2013).
53. Rao, S. A. & Yamagata, T. Abrupt termination of Indian Ocean dipole events in response to intraseasonal disturbances. *Geophys. Res. Lett.* **31**, L19306 (2004).
54. McPhaden, M. J. et al. The tropical Ocean-Global atmosphere observing system: a decade of progress. *J. Geophys. Res. Oceans* **103**, 14169–14240 (1998).
55. Ando, K. et al. Drift characteristics of a moored conductivity–temperature–depth sensor and correction of salinity data. *J. Atmos. Ocean. Technol.* **22**, 282–291 (2005).
56. McPhaden, M. J. et al. RAMA: the research moored array for African–Asian–Australian monsoon analysis and prediction. *Bull. Am. Meteorol. Soc.* **90**, 459–480 (2009).
57. Jin, F.-F., Lin, L., Timmermann, A. & Zhao, J. Ensemble-mean dynamics of the ENSO recharge oscillator under state-dependent stochastic forcing. *Geophys. Res. Lett.* **34**, L03807 (2007).
58. Kucharski, F., Bracco, A., Yoo, J. H. & Molteni, F. Atlantic forced component of the Indian monsoon interannual variability. *Geophys. Res. Lett.* **35**, L04706 (2008).
59. Wang, C., Kucharski, F., Barimalala, R. & Bracco, A. Teleconnections of the tropical Atlantic to the tropical Indian and Pacific Oceans: a review of recent findings. *Meteorol. Z.* **18**, 445–454 (2009).
60. Zhang, G., Wang, X., Xie, Q., Chen, J. & Chen, S. Strengthening impacts of spring sea surface temperature in the north tropical Atlantic on Indian Ocean dipole after the mid-1980s. *Clim. Dyn.* **59**, 185–200 (2022).
61. McKenna, S., Santoso, A., Gupta, A., sen, Taschetto, A. S. & Cai, W. Indian Ocean Dipole in CMIP5 and CMIP6: characteristics, biases, and links to ENSO. *Sci. Rep.* **10**, 11500 (2020).
62. Cai, W. et al. Increased variability of eastern Pacific El Niño under greenhouse warming. *Nature* **564**, 201–206 (2018).
63. Santoso, A., England, M. H. & Cai, W. Impact of Indo-Pacific feedback interactions on ENSO dynamics diagnosed using ensemble climate simulations. *J. Clim.* **25**, 7743–7763 (2012).
64. Ham, Y. G., Choi, J. Y. & Kug, J. S. The weakening of the ENSO–Indian Ocean Dipole (IOD) coupling strength in recent decades. *Clim. Dyn.* **49**, 249–261 (2017).
65. Huang, B. et al. Extended reconstructed sea surface temperature, version 5 (ERSSTv5): upgrades, validations, and intercomparisons. *J. Clim.* **30**, 8179–8205 (2017).
66. Rayner, N. A. et al. Global analyses of sea surface temperature, sea ice, and night marine air temperature since the late nineteenth century. *J. Geophys. Res. Atmospheres* **108**, 4407 (2003).
67. Reynolds, R. W., Rayner, N. A., Smith, T. M., Stokes, D. C. & Wang, W. An improved in situ and satellite SST analysis for climate. *J. Clim.* **15**, 1609–1625 (2002).
68. Zuo, H., Balmaseda, M. A., Tietsche, S., Mogensen, K. & Mayer, M. The ECMWF operational ensemble reanalysis–analysis system for ocean and sea ice: a description of the system and assessment. *Ocean. Sci.* **15**, 779–808 (2019).
69. Carton, J. A., Chepurin, G. A. & Chen, L. SODA3: a new ocean climate reanalysis. *J. Clim.* **31**, 6967–6983 (2018).
70. Behringer, D. et al. Evaluation of the global ocean data assimilation system at NCEP: The Pacific Ocean. *Proc. Eighth Symp. on integrated observing and assimilation systems for atmosphere, oceans, and land surface*, AMS 84th annual meeting in Washington State Convention and Trade Center, Seattle, Washington, 11–15 January 2004, Am. Meteorol. Soc., 2.3.,11–15 (2004).

ACKNOWLEDGEMENTS

This work was supported by National Research Foundation of Korea (NRF) grants funded by the Korean government (MSIT) (NRF-2018R1A5A1024958, RS-2023–00208000), and by the Yonsei Signature Research Cluster Program of 2021 (2021-22-0003). A.S. was supported by Australian Government's National Environmental Science Program.

AUTHOR CONTRIBUTIONS

S.-I.A. initiated and led this research. H.-J.P. performed the analyses. H.-J.P. and S.-K.K. developed the analysis method. All authors participated in discussions and contributed to the writing.

COMPETING INTERESTS

The authors declare no competing interests.

ADDITIONAL INFORMATION

Supplementary information The online version contains supplementary material available at https://doi.org/10.1038/s41612-023-00422-2.

Correspondence and requests for materials should be addressed to Soon-Il An.

Reprints and permission information is available at http://www.nature.com/reprints

Publisher's note Springer Nature remains neutral with regard to jurisdictional claims in published maps and institutional affiliations.